Author/s:
Schwarz, KN;Mitchell, VD;Khan, SUZ;Lee, C;Reinhold, A;Smith, TA;Ghiggino, KP;Jones, DJ;Rand, BP;Scholes, GD

Title:
Morphological Requirements for Nanoscale Electric Field Buildup in a Bulk Heterojunction Solar Cell

Date:
2021-01-14

Citation:
Schwarz, K. N., Mitchell, V. D., Khan, S. U. Z., Lee, C., Reinhold, A., Smith, T. A., Ghiggino, K. P., Jones, D. J., Rand, B. P. & Scholes, G. D. (2021). Morphological Requirements for Nanoscale Electric Field Buildup in a Bulk Heterojunction Solar Cell. Journal of Physical Chemistry Letters, 12 (1), pp.537-545. https://doi.org/10.1021/acs.jpclett.0c03425.

Persistent Link:
https://hdl.handle.net/11343/345176

Morphological Requirements for Nanoscale Electric Field Buildup in a Bulk Heterojunction Solar Cell

*Kyra N. Schwarz[1,3], Valerie D. Mitchell[2,3,4], Saeed-Uz-Zaman Khan[5], Calvin Lee[2,3], Adam Reinhold[1], Trevor A. Smith[3], Kenneth P. Ghiggino[3], David J. Jones[2,3], Barry P. Rand[5,6], Gregory D. Scholes[1,3]**

[1]Department of Chemistry, Princeton University, Princeton, NJ 08544, USA

[2]Bio21 Institute and [3]School of Chemistry, University of Melbourne, Parkville, VIC 3010, Australia

[4]Australian Synchrotron, 800 Blackburn Rd, Clayton, VIC 3168, Australia

[5]Department of Electrical Engineering and [6]Andlinger Center for Energy and the Environment, Princeton University, Princeton, NJ 08544, USA

AUTHOR INFORMATION

Corresponding Author

*Correspondence to: gscholes@princeton.edu

ABSTRACT

The morphology of organic semiconductors is critical to their function in optoelectronic devices and is particularly crucial in the donor–acceptor mixture that comprises the bulk heterojunction of organic solar cells. Here, energy landscapes can play integral roles in charge photogeneration, and recently have been shown to drive the accumulation of charge carriers away from the interface, resulting in the buildup of large nanoscale electric fields—much like a capacitor. In this work we combine morphological and spectroscopic data to outline the requirements for this inter-domain charge accumulation, finding that this effect is driven by a three-phase morphology that creates an energetic cascade for charge carriers. By adjusting annealing conditions, we show that domain purity—but not size—is critical for an electro-absorption feature to grow-in. This demonstrates that the energy landscape around the interface shapes the movement of charges and that pure domains are required for charge carrier buildup that results in reduced recombination and large inter-domain nanoscale electric fields.

TOC GRAPHICS

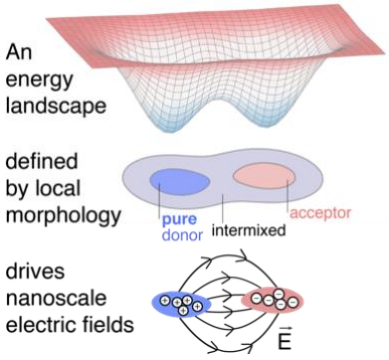

KEYWORDS

Organic semiconductor, energy landscape, organic photovoltaics, electro-absorption, Stark effect, mixed phase, transient absorption spectroscopy, morphology

Emergent optoelectronic technologies made from organic semiconductors, quantum dots and perovskites incorporate both order and disorder at the nanoscale, where understanding the relationship between structure and function is crucial for building efficient devices.[1–5] Morphology is particularly vital for the functioning of organic solar cells, where mixtures of electron donor and acceptor molecules form the basis of the bulk heterojunction (BHJ).[6,7] Since its development the BHJ has become the standard active layer structure in organic photovoltaic research where efficiencies now exceed 18%.[8] The morphology of the active layer can influence all steps of solar light harvesting; photon absorption, exciton migration to the donor–acceptor interface, charge transfer, and carrier transport to device electrodes.[9]

The energy landscape of the bulk heterojunction greatly impacts exciton and charge behavior and can be critical to solar cell operation.[10–14] Recent studies have found that the donor–acceptor interfacial energy landscape can be driven by electrostatic fields (i) between donor and acceptor molecules[15] (ii) from individual molecules with large quadrupole moments[16,17] or (iii) between regions of different molecular packing.[18–22] The energy landscape can also be defined by local differences in donor–acceptor morphology *via* phases that can induce energetic cascades for photogenerated charges.[23–28] A 'three phase' morphology has been shown to result in opposite charge-carriers generated in the intermixed phase[29–31] driven away from the interface into pure phases,[32,33] resulting in efficient charge transfer and reduced recombination.[34–37]

We have recently reported an emergent bulk heterojunction property driven by energy landscapes—the appearance of nanoscale carrier accumulation between domains and significant capacitor-like electric field buildup.[38] This effect has been observed in BQR (benzodithiophene-quaterthiophene-rhodanine) electron donor and $PC_{71}BM$ ([*6,6*]-phenyl-C_{71} butyric acid methyl ester) acceptor blends (see structures in Figure 1**a**), where free carriers accumulate in their

respective domains on the nanosecond timescale giving rise to large (> 480 V/cm) electric fields between local nanoscale regions of positive and negative charge. Nanoscale electric fields have been implicated in charge behavior and chemical reactivity in a variety of settings,[19,39–41] and here we find that fields are consistent with suppression of bimolecular recombination, a remarkable 2000-fold reduction compared to the Langevin rate.[38] These electric fields are thought to drive high steady-state carrier densities as a function of local nanoscale morphology, increasing quasi-Fermi level splitting, photocurrent production, and open-circuit voltage. Charge carrier buildup shows that carriers are held away from the interface on pico- to nanosecond timescales reducing recombination, but this effect dissipates on microsecond timescales where carriers are able to migrate to electrodes.[38]

Electric fields caused by photoinduced charges following the energy landscape are large enough to measurably perturb the absorption of surrounding ground state chromophores. This can be detected using transient absorption spectroscopy and is identified by its Stark signature,[42,43] a signal that has been described as an *ultrafast voltmeter*.[44] A Stark effect involves an electric field acting on a molecule undergoing a transition between electronic states, interacting with either its change of polarizability or change of dipole moment. A change of polarizability will induce a dipole moment only in the direction of the electric field regardless of the molecule's orientation, resulting in an electro-absorption (EA) signal that has a lineshape equal to the first derivative of the ground state absorption spectrum.[42] A Stark effect that is instead dominated by the transition dipole moment can result in either a first or second derivative signal depending on orientational effects (Figure 1**b**). Here an isotropic distribution of relative orientations between chromophores' transition dipole moments, $\Delta\mu$, and an electric field leads to transitions that shift to both higher

and lower energies, resulting in a second derivative lineshape of the EA signature[42,43] (see Figure 1**c**).

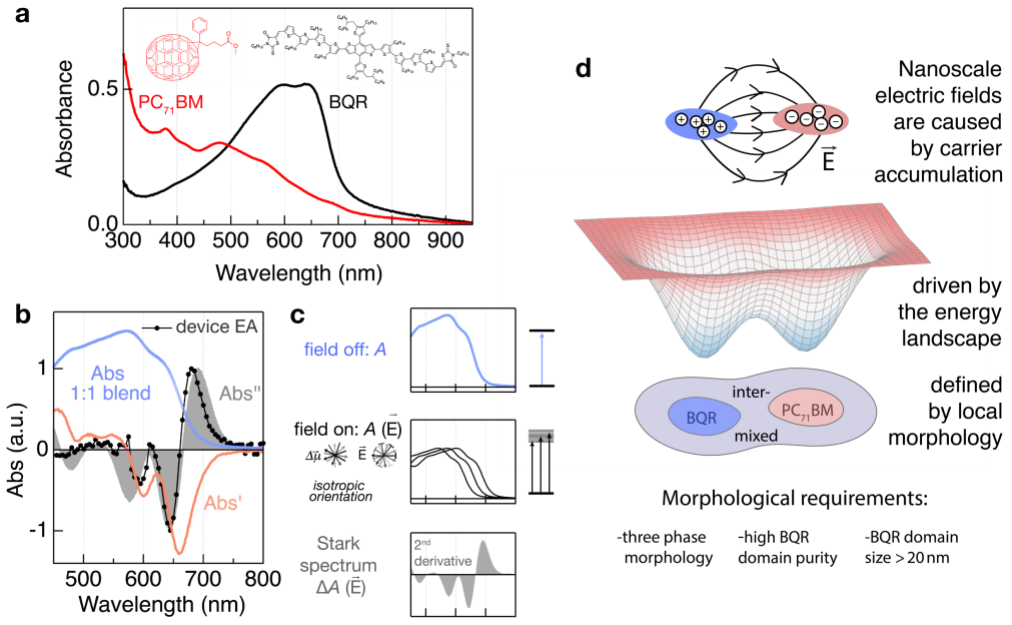

Figure 1a. Molecular structures and ground state absorbance spectra of BQR and $PC_{71}BM$ films. **b**. The absorption spectrum of a 1:1 BQR:$PC_{71}BM$ blend after 20 s of solvent vapor annealing (SVA), showing the first and second derivative of this absorption spectrum. The device electro-absorption spectrum is shown in black, where a voltage is applied via electrodes to the blend film. Here, the electro-absorption response is dominated by the change in dipole moment, $\Delta\mu$, with the applied field, E. **c**. explains how an electric field can produce the 2nd derivative of the absorption spectrum *via* the Stark effect. Here, the change in dipole moment with electric field shifts the energy levels of the molecule, where a variety of relative orientations between transition dipole moment and electric field broadens the 'field on' absorption, and the difference between 'field on' and 'field off' gives a second derivative lineshape. **d.** Nanoscale electric fields in these systems are caused by charge carrier build-up. This is driven by the energy landscape and defined by a local morphology that is the subject of this work.

The nanoscale electric fields that cause an EA signature in nearby ground-state molecules are ultimately caused by the charge accumulation of free carriers defined by the local energy landscape (see Figure 1**d**). Energy landscapes have also been the subject of increasing recent attention for their role in overcoming large Coulomb barriers to charge separation in organic solar cells,[16,22,28,45] and for driving counterintuitively beneficial local charge accumulation in perovskite devices.[46] Enhancing the understanding between semiconductor nanostructure and key

optoelectronic and/or electrostatic processes is crucial for designing strategies that ultimately optimize the potential of these technologies.

In this work, we report a systematic study of blend morphology and dynamics to unravel and clarify the requirements for nanoscale capacitive charging in a bulk heterojunction. By altering annealing conditions and donor-acceptor content, the impact of blend morphology on nanoscale electric field buildup is probed by the photoinduced electro-absorption signal it produces in transient absorption spectroscopy. We find that a three-phase morphology defines the energy landscape (Figure 1**d**) and is a key requirement for electric fields to build up locally across interfaces. We also identify that a threshold domain purity must be reached—irrelevant of domain size—to turn on the nanoscale charge accumulation phenomenon.

We first investigate a variety of donor–acceptor blend ratios. Previous work[38] on this system determined that as-cast films of 1:1 BQR:$PC_{71}BM$ generate excitons that form free carriers, though these carriers recombined bimolecularly and ultimately form BQR triplet excitons (Figure S1**a**). In contrast, identical films that had undergone 20 s of solvent vapor annealing (SVA) did not show the triplet loss channel (Figure S1**b**), with reduced bimolecular recombination that was 2000 times reduced from the predicted Langevin factor. These SVA films also showed a significant electric field buildup on the 100 ps timescale, in the form of a growing second derivative Stark signature after carrier separation was complete.

Here, we vary blend composition from 5% to 95% donor content by weight with identical annealing conditions (20 s SVA) with absorption and emission spectra illustrated in Figure 2**a**. Blends of only 5% donor or acceptor are likely to be in the dilute regime,[47] where the majority of each component material is fully miscible with the other. With increasing BQR content, the

absorption spectra feature a grow-in of the BQR vibronic shoulder indicating increasing aggregation and a decrease of the $PC_{71}BM$ content evident in the higher energy region of the spectra.

The emission observed from these films has a peak at ~760 nm (Figure 2**a** right, dashed lines) and is due to the fluorescence of BQR excitons. This emission is largely quenched when incorporated into a blend with the $PC_{71}BM$ acceptor, showing that excitons undergo charge transfer at the donor-acceptor interface in a well-mixed film morphology. The emission of BQR in these blends is significantly suppressed for ratios of 40% BQR and below, indicating that excitons are quenched by either small domains or significant donor–acceptor intermixing.

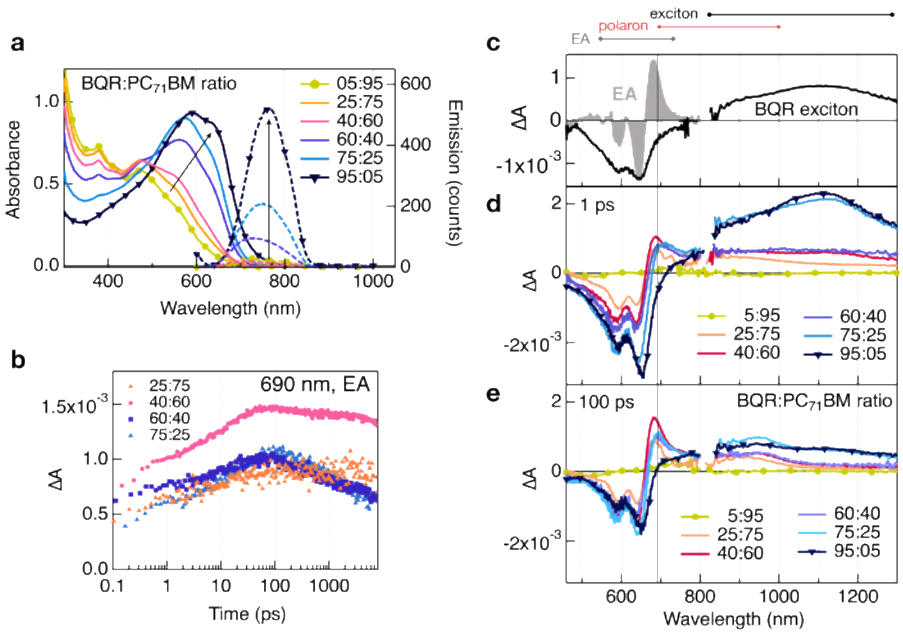

Figure 2. The impact of donor–acceptor blend ratios on the opto-electronic and spectroscopic properties of BQR:$PC_{71}BM$ blends with 20 s solvent vapor annealing. **a** shows the absorption (left) and emission (right, dashed) spectra of BQR:$PC_{71}BM$ blend films in different blend ratios where the arrow indicates an increase in BQR donor content. **b** The electro-absorption buildup at 690 nm of BQR:$PC_{71}BM$ blends of donor: acceptor ratios of 25:75, 40:60, 60:40 and 75:25. **c.** Spectra are shown of the BQR exciton, taken from a neat film of BQR at 100 ps, and of the BQR electro-absorption, taken from a blend film with a voltage applied. BQR:$PC_{71}BM$ blend film transient spectra are shown after **d**. 1 ps delay and **e.** 100 ps delay with BQR:$PC_{71}BM$ ratios of 5:95, 25:75, 40:60, 60:40, 75:25 to 95:05. Spectra and dynamics of each blend are shown in Supporting Information Figure S3 and Figure S4.

Transient absorption spectroscopy allows the populations of excitons and polarons, and also the buildup of interdomain electric field to be tracked—see Figure 2**c** and Figure S2 for component spectra. The interdomain electric field can be monitored via the 2nd derivative shaped electro-absorption (EA) signature. In Figure 2**d**–**e**, all blend data show the BQR exciton feature at early times—as a photoinduced absorption (PA) from 850–1300 nm as in the neat BQR film, though this is limited in the 5:95 BQR:$PC_{71}BM$ blend which has low absorption when excited at 600 nm. As previously reported,[38] a characteristic BQR hole polaron signature stretches over the spectral region from 700–1000 nm. In all blends, excitons form polarons within ~0.2 ps (see Supporting Information, Figure S3–S4) that persist as long-lived species beyond the 7 ns time delay of this experiment. Even when $PC_{71}BM$ content is reduced to ~5%, efficient charge generation occurs, as

acceptor molecules are well-distributed in the blend.[48] Blend ratios of 25:75, 40:60 and 60:40 all have their large exciton signal significantly quenched within 100 ps (Figure 2**e**).

In addition to these signals, we observe the characteristic 2nd derivative electro-absorption (EA) signature in the blends with 25% to 75% relative BQR donor content. Here, as previously investigated,[38] excitons form polarons at early times followed by a slower growing electro-absorption signature that builds as carriers migrate to pure domains. The electro-absorption signal is quite tolerant to changes to the blend composition, however, a clear difference is observed when the donor or acceptor content is decreased to only 5%. The 95:5 blend illustrates this with a large initial population of excitons (PA from 850–1300 nm) forming charge carriers (PA from 700–1000 nm) but unlike the other blend ratios, the electro-absorption signature and grow-in is completely missing from these spectra, see Figure 2**e**. This shows that a morphology with completely isolated $PC_{71}BM$ molecules does not support the buildup of an electro-absorption signal and electric fields between charge carriers across domains. This observation is likely explained by the lack of a three-phase morphology in this system, i.e. two pure phases and an intermixed phase, which is required to drive the energetic cascade[2,48] of charge carriers to form electric fields between domains.

Transient absorption kinetic traces of excitons, polarons and the EA are shown in Figure 2**b** and Supporting Information Figure S4. The EA signal dynamics can be tracked at its peak at 690 nm, indicating the buildup of an electric field over hundreds of picoseconds that is caused by the migration of free carriers to ordered domains.[38]

To further investigate the morphology and size of domains that cause electric field buildup, we apply annealing conditions to further alter the donor–acceptor blend character. Thermal annealing has been known to improve device performance in a number of organic photovoltaic blends and is

generally found to increase domain sizes with increasing annealing time and temperature. Figure 3**a** shows the effect of thermal annealing on the absorption and emission of 1:1 BQR:$PC_{71}BM$ blends. Annealing for 10 min at either 120 °C or 160 °C gives rise to increases in the vibronic shoulder in the absorption spectrum, consistent with increased BQR π–π stacking which is enhanced compared to both the as-cast and 20 s SVA blends. The BQR emission increases in the annealed blends compared to the as-cast film (i.e. is less quenched), and is higher with 120 °C and 160 °C annealing than the SVA treatment with THF (Figure 3**b**). This indicates that larger domains are formed that also have sufficient purity to leave BQR excitons unquenched and able to fluoresce, though this emission acts as an additional loss pathway.

Grazing incidence wide angle x-ray scattering (GIWAXS) offers insight into the change of molecular ordering within films. The GIWAXS data show an increase in crystallinity with higher temperature thermal annealing treatment (Figure 3**c**), and confirm that thermally annealed films have larger crystallites indicative of larger pure domains relative to those annealed with solvent vapor (see Figure 3**b** and Supporting Information Figure S6 and Table S1). Blends annealed at 120 °C and 160 °C have on average 40 nm and 79 nm crystallite coherence lengths (CCLs) respectively. In contrast to GIWAXS, grazing incidence small angle x-ray scattering (GISAXS) interrogates larger morphological features directly. Analysis of GISAXS for the SVA blend films (see Table S2 and Figure S5) show a clear peak that we identify as the long period, which is commonly associated with domain size. A shift of this peak to lower scattering vector *q* indicates an increase in size of the corresponding thin-film structure. In SVA films, this scattering peak denotes a domain size of 30 nm, while thermal annealing at 120 ˚C increases the domain size to 50 nm (Table S2). Annealing the film at 160 ˚C shifts the peak beyond the low limit of the measurement, indicating domain sizes upwards of 125 nm (Table S2).

Transient absorption data in Figure 3**d**–**f** again reveal the appearance and buildup of a large electro-absorption feature in both thermally annealed films (see Supporting Information Figures S7-S8 for full spectra and dynamics). Figure 3**d** shows that the magnitude of the EA signal is similar in both thermally annealed films, but the buildup time is more gradual in the film annealed at the lower 120 °C temperature due to the amount of intermixed phase in the different blends. Charge carriers generated in the intermixed phase must migrate to aggregate domains in order to accumulate carriers and build up an electric field between nanoscale domains. However, in the 160 °C annealed film with a higher amount of crystallinity and larger domains, less intermixed phase also ensures that the electro-absorption buildup duration is not as significant, where carriers can

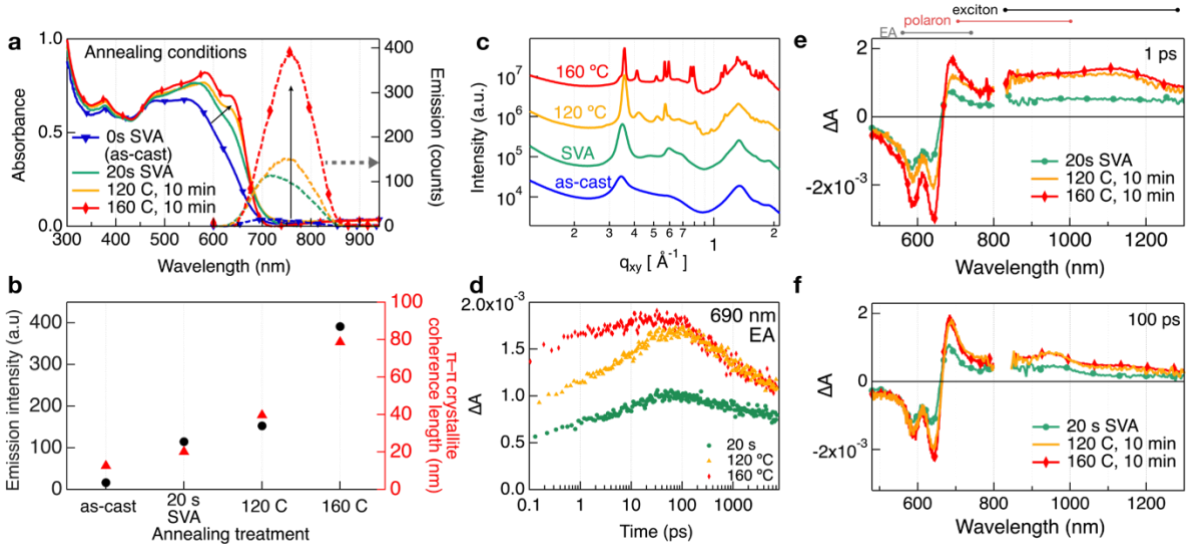

Figure 3. The evolution of opto-electronic, spectroscopic and structural properties of BQR:$PC_{71}BM$ blends with thermal annealing. **a**. shows the absorption (left) and emission (right) spectra of 1:1 BQR:$PC_{71}BM$ blend films after different annealing methods and temperatures. The maximum intensity of this emission is plotted as a function of annealing treatment in **b** (left), along with the GIWAXS π–π crystallite coherence length as a function of annealing treatment (right). **c**. GIWAXS in-plane line profiles show the change in crystallinity for each annealing treatment. **d.** The transient absorption kinetics of the electro-absorption signature in solvent and thermally annealed samples. **e**. BQR:$PC_{71}BM$ blend films after 1 ps delay and SVA time of 20 s and thermal annealing for 10 min at 120 °C and 160 °C. **f.** BQR:$PC_{71}BM$ blend films after 100 ps delay and solvent vapor annealing time of 20 s and thermal annealing for 10 min at 120 °C and 160 °C.

create electric fields promptly across an interface without needing to migrate through large amounts of intermixed material.

We show here a significant EA signal in samples with donor domains of 20 nm through to 120 nm, demonstrating that inter-domain electric field buildup is not caused by domains of a specific size. Consistently, the purity of these BQR domains is high, as illustrated by their emission (Figure 3**a**) and x-ray scattering intensity (see Fig. S6). This would suggest that the intermixed donor–acceptor interfacial region appears to drives charge accumulation dictated by the energy landscape, regardless of domain size if above the 20 nm threshold.

Finally, we investigate the morphology that leads to charge accumulation as a function of SVA time. Figure 4**a** shows the absorption (left) and emission (right) of 1:1 BQR:$PC_{71}BM$ blend films with increasing exposure times for SVA with THF. The optical properties of BQR are sensitive to changes in molecular arrangement; the as-cast blend features a larger proportion of molecularly

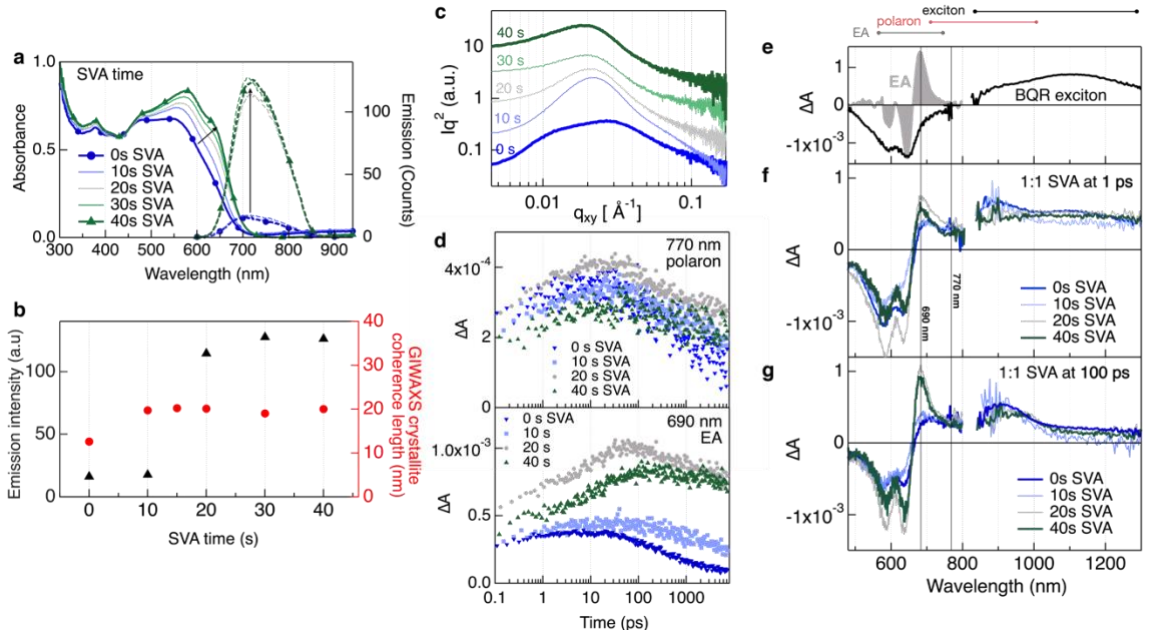

Figure 4. The impact of SVA with THF on morphological, optical and electro-absorption characteristics of BQR:$PC_{71}BM$ blends. **a**. shows the absorption spectra (left) and emission (right) of 1:1 BQR:$PC_{71}BM$ blend films after different SVA times. **b.** shows the maximum emission intensity from **a**, (left) along with the GIWAXS π–π crystallite coherence length (right) as a function of annealing time. **c.** GISAXS analysis of domain size as a function of SVA time. In **d**, (upper) the dynamics of the polaron at 770 nm and (lower) electro-absorption (690 nm) are shown for each SVA time. **e**. Spectra for comparison of the BQR exciton, taken from a neat film of BQR, and of the BQR electro-absorption, taken from a blend film with a voltage applied. **f.** BQR:$PC_{71}BM$ blend films after 1 ps pump-probe delay and SVA times of 0 s, 10 s, 20 s and 40 s. **g.** BQR:$PC_{71}BM$ blend films after 100 ps delay and SVA times of 0 s, 10 s, 20 s and 40 s, where a clear difference in the EA signature is observed between samples with 10 s and 20 s annealing time.

disordered BQR molecules compared to annealed samples, with the bulky fullerene preventing BQR molecular ordering. During SVA, the BQR 0-0 and 0-1 vibronic peaks steadily increase, typical of BQR aggregate formation in the blend. The BQR emission (Figure 4**a**, right) is largely quenched when incorporated into a blend with the $PC_{71}BM$ acceptor, showing that excitons undergo charge transfer at a donor-acceptor interface in a well-mixed film morphology. This is observed for emission from the as-cast blend film with 0 s SVA (Figure 4**a**-**b**) and also for the blend film following 10 s of SVA time. Between 10 and 20 seconds of exposure to THF vapor, BQR domains undergo a change, leading to a significant increase in emission intensity, pointing to domains of higher purity where not all excitons can diffuse to reach the donor–acceptor interface and be quenched. This emission remains consistent for longer SVA times, where pure domains form and remain a similar size and purity rather than becoming larger over time. The benefits from pure domains outweigh the emissive exciton losses as has been observed in BQR devices and many OPV material blends.[1,49]

The GIWAXS data (see Supporting Information Figure S6) show sharper reflections for the BQR donor with increasing SVA time, with a distinct increase between 0 and 10 s annealing. We do not observe a monotonic increase in the BQR π–π CCL with increasing SVA time (see Figure 4**b** and Table S1), which would indicate an incremental increase of donor crystallite size with annealing. Rather, we observe an increase in π–π CCL between 0 and 10 s of SVA, followed by a plateau at ~20 nm for all other SVA times. We also note that GIWAXS data show that face-on and edge-on populations are very similar, consistent with 3-dimensional pathways for charge percolation between domains. For the acceptor material, a broad 1.3 $Å^{-1}$ peak indicates the presence of amorphous $PC_{71}BM$ aggregates. With any annealing treatment, this peak

sharpens/narrows indicating an increase in aggregation and greater amount of amorphous $PC_{71}BM$ phase, though a crystalline $PC_{71}BM$ phase is not observed in any samples.

This observation is supported by our examination of domain sizes as determined by the position of the long period reflection in GISAXS (Figure 4**c**, Table S2). The domain sizes are remarkably similar across the treatment range from as-cast to the maximum SVA duration, increasing only slightly from 27 nm in size to 28 nm in the first 15 s, and up to 33 nm after 40 s. This is in contrast to the GIWAXS CCLs (see Figure 4**b** and Table S1), which increase notably in the first 10 s of SVA, from 13 nm to 21 nm. This suggests that while domain sizes remain relatively static in the first 15 s, there is a significant enhancement in domain purity.

We correlate these morphological data with the dynamics and spectra associated with charge carriers and the electro-absorption signature of the blend (Figure 4**d**–**g** and Supporting Information Figure S9–10 for full spectra and dynamics). There is no apparent EA signature in blend films with 0 s or 10 s of SVA. The EA signature appears to 'switch on' in samples with 20 s and longer SVA time. For all samples, the polaron photoinduced absorption dynamic (Figure 4**d** upper) indicates the immediate generation of charges in the intermixed phase after photoexcitation, with a slower charge generation (~5 ps) mediated by exciton diffusion in pure domains. The EA can be tracked at its peak at 690 nm (Figure 4**d** lower), where its increase over 100 ps in samples with 20 s or longer SVA shows the buildup of an electric field that is caused by the migration of free carriers into lower-energy, ordered domains.

The evolution of this film structure with SVA begins with a partially phase separated morphology, with the basic domain sizes established during solution casting. Within 10 s, SVA quickly produces crystallites averaging 20 nm in coherence length, while the average domain size

as determined by GISAXS remains relatively constant. While they do not increase in size, the domains significantly increase in purity with SVA time i.e. acceptor material is expelled from BQR domains. This reaches a critical point between 10 and 20 s, similar to that observed in the recent morphological study by Bourque et al.[50] This observation is also supported by a significant step change in fluorescence intensity, and the appearance of the electro-absorption signal indicating that charges have available domains in which to accumulate in high densities. Positive charges that are generated in intermixed regions are able to migrate to pure BQR aggregate domains, which manifests as an increase in the electro-absorption signature and the substantial buildup of nanoscale electric fields. SVA leads to an enhancement in BQR aggregate species, but a step-change in domain purity. Pure domains are associated with favorable charge transport and reduced recombination in a variety of devices,[5] and here appear to be a key factor for the formation of electric fields between nanoscale domains.

In conclusion, we have used spectroscopic and x-ray data to outline the morphological requirements for nanoscale charge accumulation that is detected through an electro-absorption signal caused by photoinduced free carriers.[38] The energy landscape of the bulk heterojunction drives this effect, which can be turned on and off by changing the blend film nanomorphology. Our findings show that a three-phase morphology is required to create energetic cascades for charge carriers that ultimately cause the interdomain buildup of nanoscale electric fields. By modifying the donor-acceptor blend ratio, we find that the electro-absorption signature is fairly insensitive to blend composition but is completely turned off when the $PC_{71}BM$ content is reduced to ~5%, despite efficient charge generation. Thermal annealing produces large crystallites and illustrates that large donor domains still support an electro-absorption grow-in, further implicating the donor-acceptor interfacial region as the driver of this effect. The integral function of the

interface leaves open the question of what roles the individual donor and acceptor materials play in driving this effect and its prevalence in other systems. Exposure to increasing SVA times reveals a clear threshold for BQR domain purity necessary for the electro-absorption signature to turn on and charge accumulation to occur. Our findings open new avenues for organic solar cell design and for the further investigation of molecular and morphological factors that give rise to energy landscapes and electrostatic effects that can reduce recombination and improve device performance.

Methods

Sample and Device Preparation. BQR was prepared according to a synthetic procedure published previously.[49] To prepare neat films, BQR and $PC_{71}BM$ (Nano-c, 99%) were first dissolved in chloroform (HPLC-grade) to a concentration of 10 mg/mL. To prepare blend films, solutions of BQR and $PC_{71}BM$ were prepared by dissolving each material in chloroform to a concentration of 20 mg/mL (to give film thicknesses of ~140 nm) and then combining solutions in the indicated ratios. Substrates were cleaned by sonicating sequentially in 1M NaOH, distilled water, acetone, isopropanol, and dichloromethane, followed by 15 min of UV/ozone treatment. All films were cast onto clean glass substrates via spin coating at 1000 rpm (2000 acceleration) for 30 s. Substrates were suspended above a glass Petri dish containing 1 mL THF for SVA.

Steady-state Spectroscopy. Absorption spectra of all films were recorded using a Varian Cary 50 UV−Vis spectrophotometer. Fluorescence spectra were recorded on a Varian Eclipse spectrofluorimeter using an excitation wavelength of 540 nm, where all spectra were corrected.

Transient Absorption. Ultrafast transient absorption measurements were conducted using a 1 kHz Ti:sapphire regenerative amplifier system (Coherent Libra) with an output of 800 nm pulses

with ~45 fs pulsewidth and approximately 4 W power. The pump arm of the Libra output was directed to an optical parametric amplifier (Light Conversion OPerA), and thereby converted into 600 nm pulses. The probe arm of the Libra output was directed to a commercial transient absorption spectrometer (Ultrafast System, Helios) and was used in the generation of visible and NIR continua, from ~450−800 nm and 800−1500 nm respectively. Optical filters were incorporated in order to separate out excess 800 nm remaining from the continua generation. Referencing of the probe spectra using a second camera was required to achieve adequate signal−to−noise at low pump fluence. The pump beam spot size was measured by analyzing the image obtained by a digital CCD camera (Thorlabs Inc.) with Thorcam Software placed at the pump probe overlap. The size of the pump beam at ca. 600 nm was approximately 3.8×10^{-3} cm^2. The pump power was measured with a high-sensitivity optical power sensor (Coherent, Santa Clara, California). Incident pump power in the visible was ~19 nJ per pulse, giving a pump fluence of 5 $\mu J/cm^2$.

For all measurements, unless otherwise indicated, an excitation density of 5 $\mu J/cm^2$ was used, to prevent artifacts associated with exciton−exciton[51] and exciton−charge annihilation[52,53]. The relative orientation of pump and probe polarization was 54.7° (magic angle) and all spectra were corrected for the chirp of the supercontinuum probe.

Grazing Incidence Wide Angle and Small Angle X-ray Spectroscopy (GIWAXS & GISAXS). GIWAXS and GISAXS measurements were conducted at the SAXS/WAXS beamline of the Australian synchrotron. The substrates were silicon wafers that had been sonicated in acetone and isopropanol for 30 min each followed by 15 min of UV/ozone treatment. The measurements were performed with an X-ray energy of 11 keV and a range of incident angles from

Ω = 0.025−0.5 in 0.01−0.05 increments to allow signal optimization near the critical angle of the polymer film but below the critical angle of the substrate. Data from GIWAXS experiments were analyzed using a customized version of NIKA 2D based in IgorPro. Crystallite coherence lengths were determined from GIWAXS data using a Scherrer analysis of the (100) lamellar reflection. GISAXS data were analyzed with horizontal linecuts along the q_{xy} axis, at incident angles slightly larger than the measured critical angle to minimize dynamic scattering effects.

Steady-state Electro-absorption Measurements. Electro-absorption (EA) samples were fabricated on patterned ITO substrates (Colorado Concept Coatings). 10 mg/mL BQR:$PC_{71}BM$ 1:1 (w:w) solution was prepared in chloroform and spun (1000 rpm, 30 s) on the ITO substrates, followed by thermal annealing at 100 °C for 10 min. Subsequently, 10 nm bathocuproine and 100 nm Al were thermally evaporated on the BQR:$PC_{71}BM$ films to complete the EA devices.

We measured the 2^{nd} harmonic EA signal of the device in reflection mode. During the measurement, direct reflected light from the Al back contact was detected in a Si detector. The device was kept under 1 V_{dc} reverse bias to minimize charge injection. Superimposed on the DC, a 1 kHz sinusoidal modulating voltage of 3 V amplitude was applied on the device and the difference in reflection due to the modulating bias was detected by connecting the Si detector output to a lock-in-amplifier (Stanford Research Systems, SR830), through a low noise current preamplifier (Stanford Research Systems, SR570).

AUTHOR INFORMATION

Notes

The authors declare no competing financial interests.

ACKNOWLEDGMENTS

G.D.S and K.N.S. acknowledge support by the U.S. Department of Energy, Office of Science, Office of Basic Energy Sciences Solar Photochemistry program under Award Number DE-SC0015429. K.N.S., K.P.G and T.A.S. acknowledge support from the ARC Centre of Excellence in Exciton Science (CE170100026). S.U.Z.K. and B.P.R. acknowledge funding from the U.S. Department of Energy, Office of Basic Energy Sciences, Division of Materials Sciences and Engineering under Award Number DE-SC0012458. This work was made possible by support from the Australian Renewable Energy Agency, which funds the project grants within the Australian Centre for Advanced Photovoltaics. GIWAXS and GISAXS were performed at the SAXS/WAXS beamline of the Australian Synchrotron. K.N.S would like to thank Bryan Kudisch for helpful discussions.

ASSOCIATED CONTENT

Supporting Information Available.

Figures S1-S10. Tables S1-S2

REFERENCES

(1) Collins, S. D.; Ran, N. A.; Heiber, M. C.; Nguyen, T.-Q. Small Is Powerful: Recent Progress in Solution-Processed Small Molecule Solar Cells. *Adv. Energy Mater.* **2017**, *7* (10), 1602242.

(2) Vandewal, K.; Himmelberger, S.; Salleo, A. Structural Factors That Affect the Performance of Organic Bulk Heterojunction Solar Cells. *Macromolecules* **2013**, *46* (16), 6379–6387.

(3) Petrus, M. L.; Schlipf, J.; Li, C.; Gujar, T. P.; Giesbrecht, N.; Müller-Buschbaum, P.; Thelakkat, M.; Bein, T.; Hüttner, S.; Docampo, P. Capturing the Sun: A Review of the Challenges and Perspectives of Perovskite Solar Cells. *Adv. Energy Mater.* **2017**, *7* (16), 1700264.

(4) Pietryga, J. M.; Park, Y.-S.; Lim, J.; Fidler, A. F.; Bae, W. K.; Brovelli, S.; Klimov, V. I. Spectroscopic and Device Aspects of Nanocrystal Quantum Dots. *Chem. Rev.* **2016**, *116* (18), 10513–10622.

(5) Zhao, F.; Wang, C.; Zhan, X. Morphology Control in Organic Solar Cells. *Adv. Energy Mater.* **2018**, *8* (28), 1703147.

(6) Yu, G.; Gao, J.; Hummelen, J. C.; Wudl, F.; Heeger, A. J. Polymer Photovoltaic Cells: Enhanced Efficiencies via a Network of Internal Donor-Acceptor Heterojunctions. *Science* **1995**, *270* (5243), 1789–1791.

(7) Halls, J. J. M.; Walsh, C. A.; Greenham, N. C.; Marseglia, E. A.; Friend, R. H.; Moratti, S. C.; Holmes, A. B. Efficient Photodiodes from Interpenetrating Polymer Networks. *Nature* **1995**, *376* (6540), 498–500.

(8) Liu, Q.; Jiang, Y.; Jin, K.; Qin, J.; Xu, J.; Li, W.; Xiong, J.; Liu, J.; Xiao, Z.; Sun, K.; Yang, S.; Zhang, X.; Ding, L. 18% Efficiency Organic Solar Cells. *Sci. Bull.* **2020**, *65* (4), 272–275.

(9) Haugeneder, A.; Neges, M.; Kallinger, C.; Spirkl, W.; Lemmer, U.; Feldmann, J.; Scherf, U.; Harth, E.; Gügel, A.; Müllen, K. Exciton Diffusion and Dissociation in Conjugated Polymer/Fullerene Blends and Heterostructures. *Phys. Rev. B* **1999**, *59* (23), 15346–15351.

(10) Rand, B. P.; Cheyns, D.; Vasseur, K.; Giebink, N. C.; Mothy, S.; Yi, Y.; Coropceanu, V.; Beljonne, D.; Cornil, J.; Brédas, J. L.; Genoe, J. The Impact of Molecular Orientation on the Photovoltaic Properties of a Phthalocyanine/Fullerene Heterojunction. *Adv. Funct. Mater.* **2012**, *22* (14), 2987–2995.

(11) Chen, X.-K.; Ravva, M. K.; Li, H.; Ryno, S. M.; Brédas, J.-L. Effect of Molecular Packing and Charge Delocalization on the Nonradiative Recombination of Charge-Transfer States in Organic Solar Cells. *Adv. Energy Mater.* **2016**, *6* (24), 1601325.

(12) Chen, X. K.; Coropceanu, V.; Brédas, J. L. Assessing the Nature of the Charge-Transfer

Electronic States in Organic Solar Cells. *Nat. Commun.* **2018**, *9* (1).

(13) Lin, Y. H. L.; Fusella, M. A.; Rand, B. P. The Impact of Local Morphology on Organic Donor/Acceptor Charge Transfer States. *Adv. Energy Mater.* **2018**, *8* (28), 1–16.

(14) Boehm, B. J.; Nguyen, H. T. L.; Huang, D. M. The Interplay of Interfaces, Supramolecular Assembly, and Electronics in Organic Semiconductors. *J. Phys. Condens. Matter* **2019**, *31* (42).

(15) Yao, H.; Cui, Y.; Qian, D.; Ponseca, C. S.; Honarfar, A.; Xu, Y.; Xin, J.; Chen, Z.; Hong, L.; Gao, B.; Yu, R.; Zu, Y.; Ma, W.; Chabera, P.; Pullerits, T.; Yartsev, A.; Gao, F.; Hou, J. 14.7% Efficiency Organic Photovoltaic Cells Enabled by Active Materials with a Large Electrostatic Potential Difference. *J. Am. Chem. Soc.* **2019**, *141* (19), 7743–7750.

(16) Perdigón-Toro, L.; Zhang, H.; Markina, A.; Yuan, J.; Hosseini, S. M.; Wolff, C. M.; Zuo, G.; Stolterfoht, M.; Zou, Y.; Gao, F.; Andrienko, D.; Shoaee, S.; Neher, D. Barrierless Free Charge Generation in the High-Performance PM6:Y6 Bulk Heterojunction Non-Fullerene Solar Cell. *Adv. Mater.* **2020**, *32* (9).

(17) Schwarze, M.; Schellhammer, K. S.; Ortstein, K.; Benduhn, J.; Gaul, C.; Hinderhofer, A.; Perdigón Toro, L.; Scholz, R.; Kublitski, J.; Roland, S.; Lau, M.; Poelking, C.; Andrienko, D.; Cuniberti, G.; Schreiber, F.; Neher, D.; Vandewal, K.; Ortmann, F.; Leo, K. Impact of Molecular Quadrupole Moments on the Energy Levels at Organic Heterojunctions. *Nat. Commun.* **2019**, *10* (1), 2466.

(18) Heimel, G.; Salzmann, I.; Duhm, S.; Koch, N. Design of Organic Semiconductors from Molecular Electrostatics. *Chem. Mater.* **2011**, *23* (3), 359–377.

(19) D'Avino, G.; Muccioli, L.; Castet, F.; Poelking, C.; Andrienko, D.; Soos, Z. G.; Cornil, J.; Beljonne, D. Electrostatic Phenomena in Organic Semiconductors: Fundamentals and

Implications for Photovoltaics. *J. Phys. Condens. Matter* **2016**, *28* (43), 433002.

(20) Cornil, J.; Verlaak, S.; Martinelli, N.; Mityashin, A.; Olivier, Y.; Van Regemorter, T.; D'Avino, G.; Muccioli, L.; Zannoni, C.; Castet, F.; Beljonne, D.; Heremans, P. Exploring the Energy Landscape of the Charge Transport Levels in Organic Semiconductors at the Molecular Scale. *Acc. Chem. Res.* **2013**, *46* (2), 434–443.

(21) Tsiper, E. V.; Soos, Z. G. Charge Redistribution and Polarization Energy of Organic Molecular Crystals. *Phys. Rev. B - Condens. Matter Mater. Phys.* **2001**, *64* (19), 1–12.

(22) Dong, Y.; Nikolis, V. C.; Talnack, F.; Chin, Y. C.; Benduhn, J.; Londi, G.; Kublitski, J.; Zheng, X.; Mannsfeld, S. C. B.; Spoltore, D.; Muccioli, L.; Li, J.; Blase, X.; Beljonne, D.; Kim, J. S.; Bakulin, A. A.; D'Avino, G.; Durrant, J. R.; Vandewal, K. Orientation Dependent Molecular Electrostatics Drives Efficient Charge Generation in Homojunction Organic Solar Cells. *Nat. Commun.* **2020**, *11* (1), 1–9.

(23) Pfannmöller, M.; Flügge, H.; Benner, G.; Wacker, I.; Sommer, C.; Hanselmann, M.; Schmale, S.; Schmidt, H.; Hamprecht, F. A.; Rabe, T.; Kowalsky, W.; Schröder, R. R. Visualizing a Homogeneous Blend in Bulk Heterojunction Polymer Solar Cells by Analytical Electron Microscopy. *Nano Lett.* **2011**, *11* (8), 3099–3107.

(24) Treat, N. D.; Varotto, A.; Takacs, C. J.; Batara, N.; Al-Hashimi, M.; Heeney, M. J.; Heeger, A. J.; Wudl, F.; Hawker, C. J.; Chabinyc, M. L. Polymer-Fullerene Miscibility: A Metric for Screening New Materials for High-Performance Organic Solar Cells. *J. Am. Chem. Soc.* **2012**, *134* (38), 15869–15879.

(25) Collins, B. A.; Gann, E.; Guignard, L.; He, X.; McNeill, C. R.; Ade, H. Molecular Miscibility of Polymer-Fullerene Blends. *J. Phys. Chem. Lett.* **2010**.

(26) Albrecht, S.; Schindler, W.; Kurpiers, J.; Kniepert, J.; Blakesley, J. C.; Dumsch, I.; Allard,

S.; Fostiropoulos, K.; Scherf, U.; Neher, D. On the Field Dependence of Free Charge Carrier Generation and Recombination in Blends of PCPDTBT/PC 70BM: Influence of Solvent Additives. *J. Phys. Chem. Lett.* **2012**.

(27) Chen, W.; Nikiforov, M. P.; Darling, S. B. Morphology Characterization in Organic and Hybrid Solar Cells. *Energy and Environmental Science*. 2012.

(28) Graham, K. R.; Ndjawa, G. O. N.; Conron, S. M.; Munir, R.; Vandewal, K.; Chen, J. J.; Sweetnam, S.; Thompson, M. E.; Salleo, A.; McGehee, M. D.; Amassian, A. The Roles of Structural Order and Intermolecular Interactions in Determining Ionization Energies and Charge-Transfer State Energies in Organic Semiconductors. *Adv. Energy Mater.* **2016**, *6* (22), 1–9.

(29) Piris, J.; Dykstra, T. E.; Bakulin, A. a; Loosdrecht, P. H. M. Van; Knulst, W.; Trinh, M. T.; Schins, J. M.; Siebbeles, L. D. a. Photogeneration and Ultrafast Dynamics of Excitons and Charges in P3HT/PCBM Blends. *J. Phys. Chem. C* **2009**, *113* (32), 14500–14506.

(30) Howard, I. A.; Mauer, R.; Meister, M.; Laquai, F. F. Effect of Morphology on Ultrafast Free Carrier Generation in Polythiophene:Fullerene Organic Solar Cells. *J. Am. Chem. Soc.* **2010**, *132* (42), 14866–14876.

(31) Tong, M.; Coates, N. E.; Moses, D.; Heeger, A. J.; Beaupré, S.; Leclerc, M. Charge Carrier Photogeneration and Decay Dynamics in the Poly(2,7-Carbazole) Copolymer PCDTBT and in Bulk Heterojunction Composites with PC70BM. *Phys. Rev. B* **2010**, *81* (12), 125210.

(32) Mukherjee, S.; Proctor, C. M.; Bazan, G. C.; Nguyen, T. Q.; Ade, H. Significance of Average Domain Purity and Mixed Domains on the Photovoltaic Performance of High-Efficiency Solution-Processed Small-Molecule BHJ Solar Cells. *Adv. Energy Mater.*

2015, *5* (21), 1–11.

(33) Oosterhout, S. D.; Savikhin, V.; Burgers, M. A.; Zhang, J.; Zhang, Y.; Marder, S. R.; Bazan, G. C.; Toney, M. F. Absence of Mixed Phase in Organic Photovoltaic Active Layers Facilitates Use of Green Solvent Processing. *J. Phys. Chem. C* **2018**, *122* (20), 11136–11144.

(34) Jamieson, F. C.; Domingo, E. B.; McCarthy-Ward, T.; Heeney, M.; Stingelin, N.; Durrant, J. R. Fullerene Crystallisation as a Key Driver of Charge Separation in Polymer/Fullerene Bulk Heterojunction Solar Cells. *Chem. Sci.* **2012**, *3* (2), 485–492.

(35) Buchaca-Domingo, E.; Ferguson, A. J.; Jamieson, F. C.; McCarthy-Ward, T.; Shoaee, S.; Tumbleston, J. R.; Reid, O. G.; Yu, L.; Madec, M.-B.; Pfannmöller, M.; Hermerschmidt, F.; Schröder, R. R.; Watkins, S. E.; Kopidakis, N.; Portale, G.; Amassian, A.; Heeney, M.; Ade, H.; Rumbles, G.; Durrant, J. R.; Stingelin, N. Additive-Assisted Supramolecular Manipulation of Polymer:Fullerene Blend Phase Morphologies and Its Influence on Photophysical Processes. *Mater. Horiz.* **2014**, *1* (2), 270–279.

(36) Burke, T. M.; McGehee, M. D. How High Local Charge Carrier Mobility and an Energy Cascade in a Three-Phase Bulk Heterojunction Enable >90% Quantum Efficiency. *Adv. Mater.* **2014**, *26* (12), 1923–1928.

(37) Sweetnam, S.; Graham, K. R.; Ngongang Ndjawa, G. O.; Heumüller, T.; Bartelt, J. A.; Burke, T. M.; Li, W.; You, W.; Amassian, A.; McGehee, M. D. Characterization of the Polymer Energy Landscape in Polymer:Fullerene Bulk Heterojunctions with Pure and Mixed Phases. *J. Am. Chem. Soc.* **2014**, *136* (40), 14078–14088.

(38) Schwarz, K. N.; Geraghty, P. B.; Mitchell, V. D.; Khan, S.-U.-Z.; Sandberg, O. J.; Zarrabi, N.; Kudisch, B.; Subbiah, J.; Smith, T. A.; Rand, B. P.; Armin, A.; Scholes, G.

D.; Jones, D. J.; Ghiggino, K. P. Reduced Recombination and Capacitor-like Charge Buildup in an Organic Heterojunction. *J. Am. Chem. Soc.* **2020**, *142* (5), 2562–2571.

(39) Shaik, S.; Ramanan, R.; Danovich, D.; Mandal, D. Structure and Reactivity/Selectivity Control by Oriented-External Electric Fields. *Chem. Soc. Rev.* **2018**, *47* (14), 5125–5145.

(40) Aragonès, A. C.; Haworth, N. L.; Darwish, N.; Ciampi, S.; Bloomfield, N. J.; Wallace, G. G.; Diez-Perez, I.; Coote, M. L. Electrostatic Catalysis of a Diels–Alder Reaction. *Nature* **2016**, *531* (7592), 88–91.

(41) Xiong, H.; Lee, J. K.; Zare, R. N.; Min, W. Strong Electric Field Observed at the Interface of Aqueous Microdroplets. *J. Phys. Chem. Lett.* **2020**, *11* (17), 7423–7428.

(42) Boxer, S. Stark Realities. *J. Phys. Chem. B* **2009**, *112* (41), 592–602.

(43) Bublitz, G.; Boxer, S. Stark Spectroscopy: Applications in Chemistry, Biology, and Materials Science. *Annu. Rev. Phys. Chem.* **1997**, *48*, 213–242.

(44) Léonard, J.; Portuondo-Campa, E.; Cannizzo, A.; Van Mourik, F.; Van Der Zwan, G.; Tittor, J.; Haacke, S.; Chergui, M. Functional Electric Field Changes in Photoactivated Proteins Revealed by Ultrafast Stark Spectroscopy of the Trp Residues. *Proc. Natl. Acad. Sci. U. S. A.* **2009**, *106* (19), 7718–7723.

(45) Athanasopoulos, S.; Schauer, F.; Nádaždy, V.; Weiß, M.; Kahle, F. J.; Scherf, U.; Bässler, H.; Köhler, A. What Is the Binding Energy of a Charge Transfer State in an Organic Solar Cell? *Adv. Energy Mater.* **2019**, *9* (24), 1–11.

(46) Feldmann, S.; Macpherson, S.; Senanayak, S. P.; Abdi-Jalebi, M.; Rivett, J. P. H.; Nan, G.; Tainter, G. D.; Doherty, T. A. S.; Frohna, K.; Ringe, E.; Friend, R. H.; Sirringhaus, H.; Saliba, M.; Beljonne, D.; Stranks, S. D.; Deschler, F. Photodoping through Local Charge Carrier Accumulation in Alloyed Hybrid Perovskites for Highly Efficient Luminescence.

Nat. Photonics **2020**, *14* (2), 123–128.

(47) Ferguson, A. J.; Kopidakis, N.; Shaheen, S. E.; Rumbles, G. Dark Carriers, Trapping, and Activation Control of Carrier Recombination in Neat P3HT and P3HT:PCBM Blends. *J. Phys. Chem. C* **2011**, *115* (46), 23134–23148.

(48) Coffey, D. C.; Larson, B. W.; Hains, A. W.; Whitaker, J. B.; Kopidakis, N.; Boltalina, O. V.; Strauss, S. H.; Rumbles, G. An Optimal Driving Force for Converting Excitons into Free Carriers in Excitonic Solar Cells. *J. Phys. Chem. C* **2012**, *116* (16), 8916–8923.

(49) Geraghty, P. B.; Lee, C.; Subbiah, J.; Wong, W. W. H.; Banal, J. L.; Jameel, M. A.; Smith, T. A.; Jones, D. J. High Performance P-Type Molecular Electron Donors for OPV Applications via Alkylthiophene Catenation Chromophore Extension. *Beilstein J. Org. Chem.* **2016**, *12*, 2298–2314.

(50) Bourque, A. J.; Engmann, S.; Fuster, A.; Snyder, C. R.; Richter, L. J.; Geraghty, P. B.; Jones, D. J. Morphology of a Thermally Stable Small Molecule OPV Blend Comprising a Liquid Crystalline Donor and Fullerene Acceptor. *J. Mater. Chem. A* **2019**, *7* (27), 16458–16471.

(51) Stevens, M. A.; Silva, C.; Russell, D. M.; Friend, R. H. Exciton Dissociation Mechanisms in the Polymeric Semiconductors Poly(9,9-Dioctylfluorene) and Poly(9,9-Dioctylfluorene-Co-Benzothiadiazole). *Phys. Rev. B* **2001**, *63* (16), 165213.

(52) Ferguson, A. J.; Kopidakis, N.; Shaheen, S. E.; Rumbles, G. Quenching of Excitons by Holes in Poly(3-Hexylthiophene) Films. *J. Phys. Chem. C* **2008**, *112* (26), 9865–9871.

(53) Hodgkiss, J. M.; Albert-Seifried, S.; Rao, A.; Barker, A. J.; Campbell, A. R.; Marsh, R. A.; Friend, R. H. Exciton-Charge Annihilation in Organic Semiconductor Films. *Adv. Funct. Mater.* **2012**, *22* (8), 1567–1577.